

Supplementary Information for Knotting fractional-order knots with the polarization state of light

Emilio Pisanty, Gerard J. Machado, Verónica Vicuña-Hernández, Antonio Picón, Alessio Celi, Juan P. Torres and Maciej Lewenstein

Dated: 23 April 2019

This file contains the Supplementary Figures S1-S11, as well as a brief description of the Supplementary Data.



Figure S1 | 3D prints of the torus-knot topology. Models of the torus-knot beam topology of Fig. 1, printed in 3D using resin-based stereolithography (SLA) on a Formlabs Form 2 printer. 3D Prints: Xavier Menino (ICFO); Image Credits: © ICFO.

The Supplementary Data contains the files used to make the prints in Fig. S1. This supplement is a zip file that primarily contains three .stl stereolithography files (trefoil.stl, triangle.stl, and mesh.stl, for Figs. S1 (a), (b) and (c), respectively), together with the Mathematica notebook (FigureMaker3Dprints.nb) used to produce those files. (The zip file also contains copies of Fig. S1, a read-me file, and the CC BY-SA license for the collection.) The prints shown here were produced using resin-based stereolithography (SLA), but trefoil.stl and triangle.stl are likely to also be accessible to fused filament fabrication (FFF / FDM). The model in mesh.stl is somewhat more fragile and harder to print correctly, and it is less likely to be accessible to FDM fabrication.

The Supplementary Data are made available under a Creative Commons Attribution-ShareAlike 4.0 ([CC BY-SA 4.0](#)) license. We thank Xavier Menino (ICFO) for valuable assistance in designing and preparing these printable files.

These models have also been archived in the Zenodo repository, at [doi:10.5281/zenodo.2597667](https://doi.org/10.5281/zenodo.2597667).

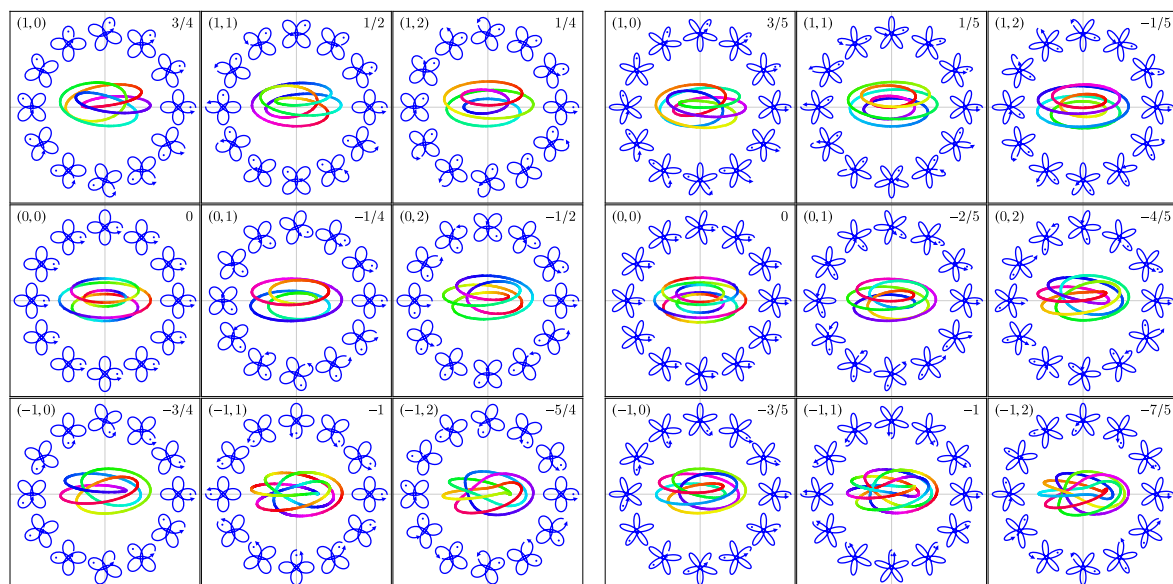


Figure S2 | Torus-knot beam topologies for different frequency ratios. Lissajous-figure fields, and the corresponding torus knots, for beams with frequency ratios $\omega : 3\omega$ (left) and $2\omega : 3\omega$ (right), plotted as in Fig. 2. In general, beam combinations of the form $p\omega : q\omega$ form Lissajous figures with $n = (p + q)$ -fold internal symmetry, and torus-knot beams with coordination parameters γ given by multiples of $1/n = 1/(p + q)$.

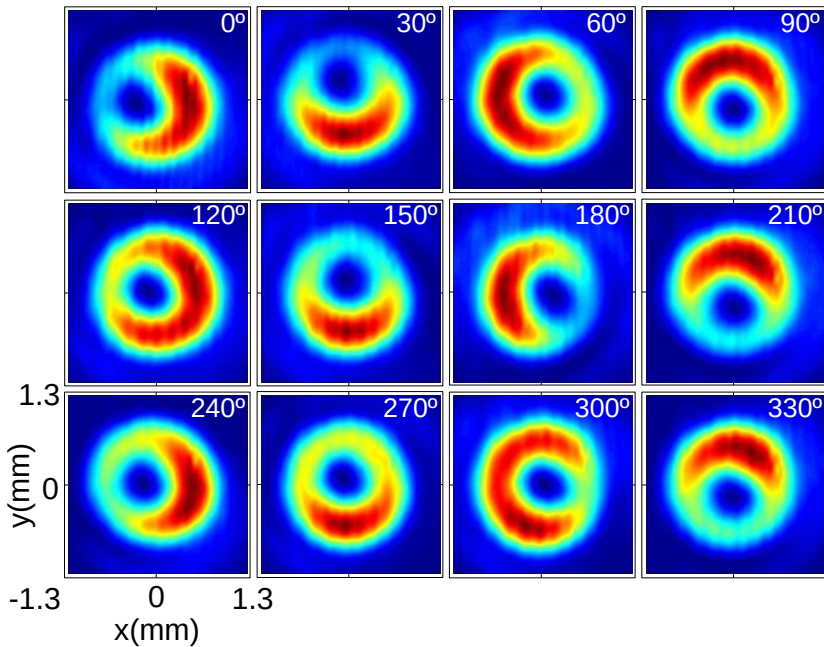


Figure S3 | Observed interference patterns. Representative interference patterns observed with $m_2 = -1$ for various values of the polarizer angle θ .

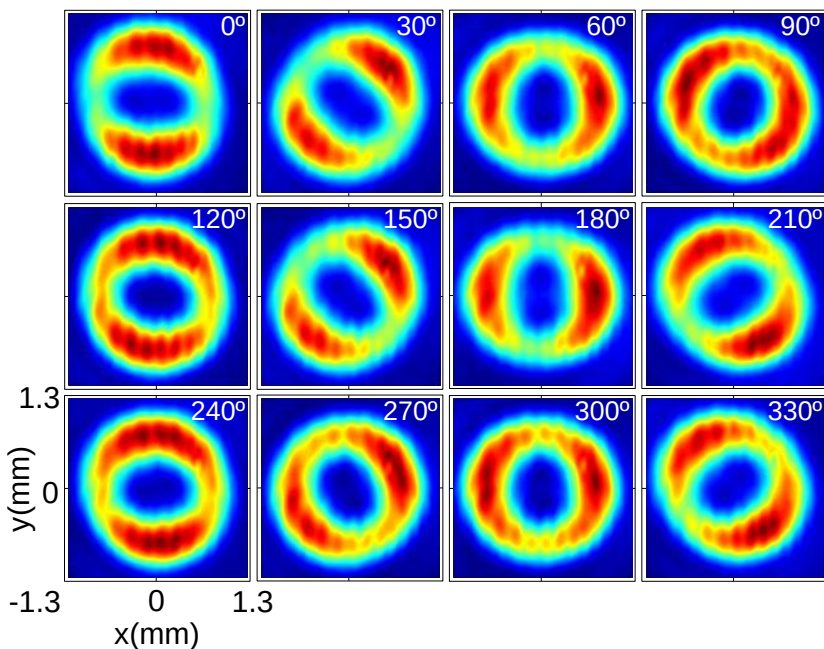


Figure S4 | Observed interference patterns. Representative interference patterns observed with $m_2 = -2$ for various values of the polarizer angle θ .

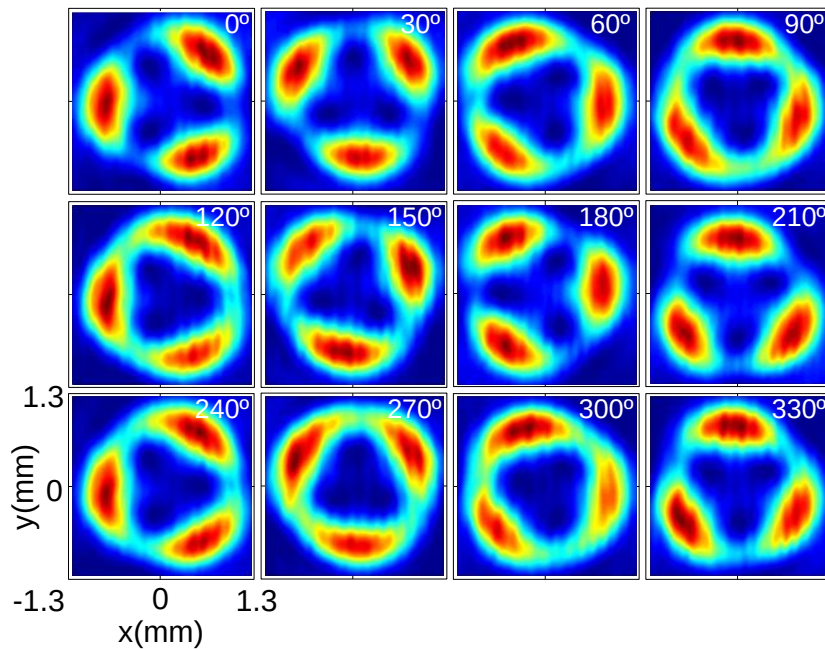


Figure S5 | Observed interference patterns. Representative interference patterns observed with $m_2 = -3$ for various values of the polarizer angle θ .

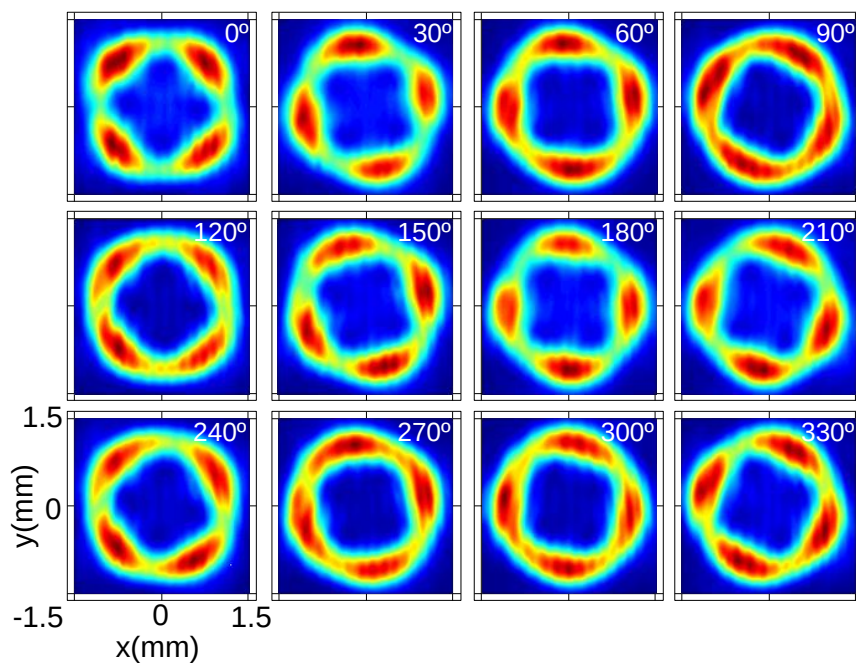


Figure S6 | Observed interference patterns. Representative interference patterns observed with $m_2 = -4$ for various values of the polarizer angle θ .

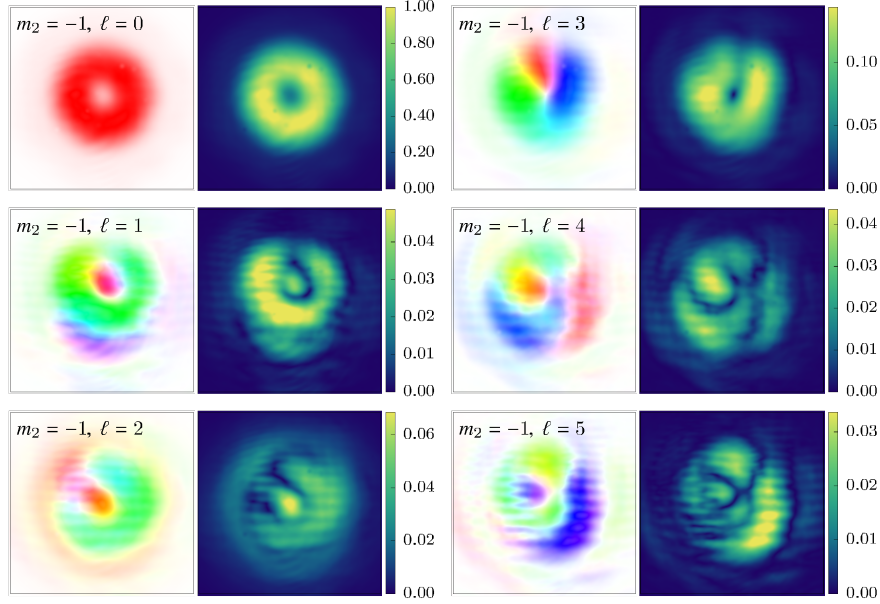


Figure S7 | Transformed experimental results. Fourier transform of the experimental results of Fig. S3, shown in both magnitude (right-hand panels) and phase (left-hand panels; $\arg(\tilde{f}_\ell(x, y))$ as the hue and $|\tilde{f}_\ell(x, y)|$ as the saturation). We normalize $|\tilde{f}_\ell(x, y)|$ to its maximum value within each plot, but we show its scale with respect to the base $\ell = 0$ intensity $|\tilde{f}_0(x, y)|$ on the density-plot tick marks. Thus, the only meaningful channel with $\ell > 0$ is $\ell = 3$, with a dominant signal and a clear phase winding.

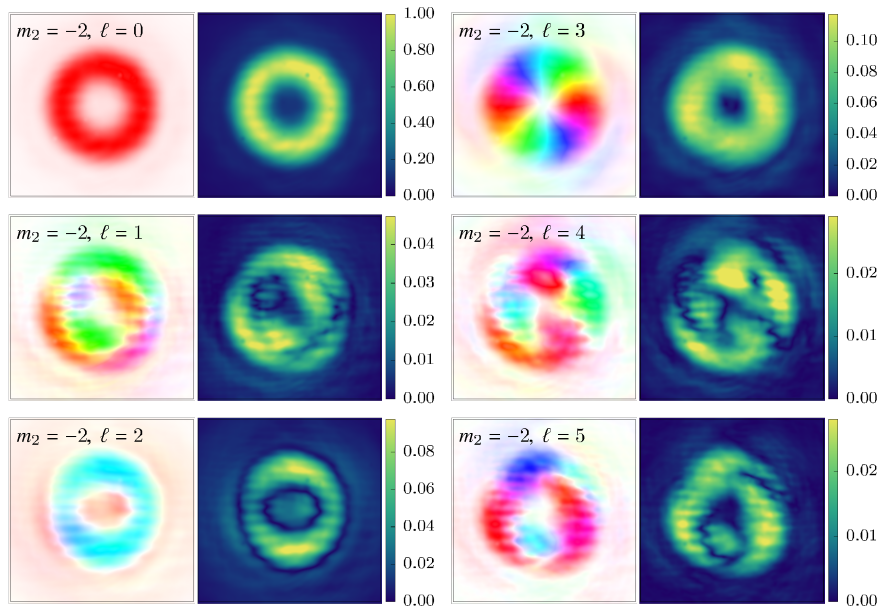


Figure S8 | Transformed experimental results. Fourier transform of the experimental results of Fig. S4 for $m_2 = -2$, plotted as in Fig. S7.

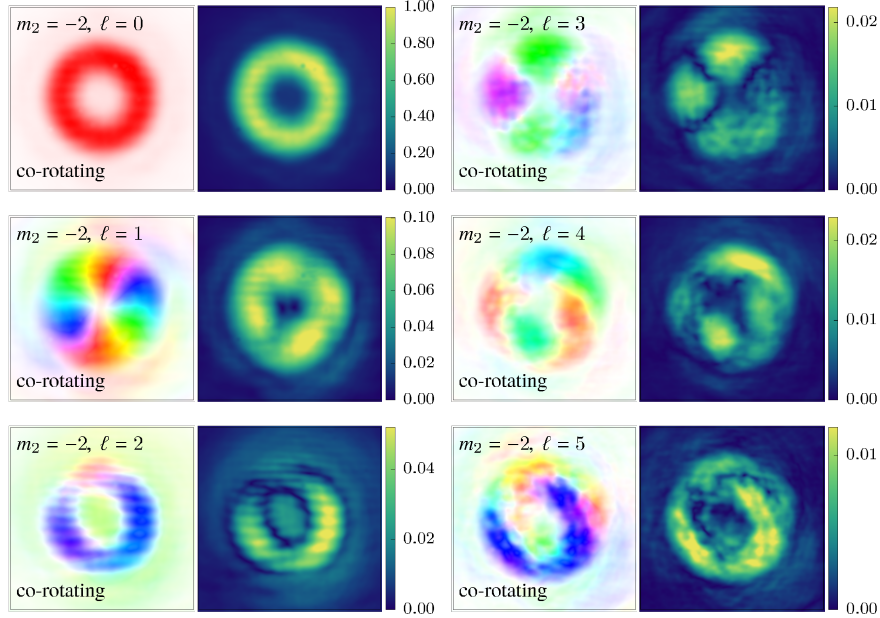


Figure S9 | Fourier analysis for co-rotating polarizations. Analysis of the results, as in Fig. S8, for co-rotating circular polarizations on both arms of the interferometer, with $m_2 = -2$. Here the dominant component shifts from $\ell = 3$ to $\ell = 1$, showing a nonzero phase winding on $T_{1,3}$, and with that a ‘true’ vector vortex.

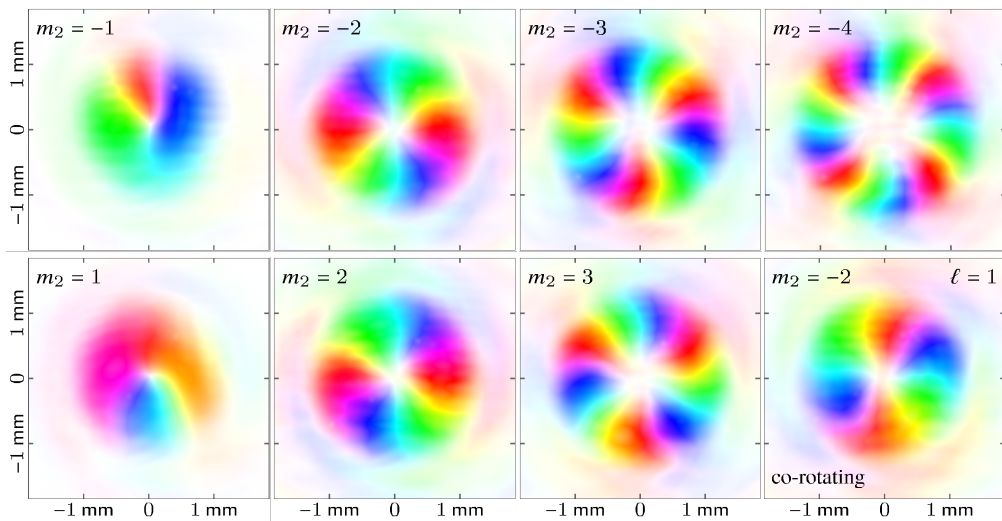


Figure S10 | Observed phase vortices. Experimentally-observed phase vortices, in $T_{3,3}$ plotted as in Figs. 3 and S7-S9, for different values of the second harmonic’s OAM m_2 , as well as for the co-rotating case of Fig. S9.

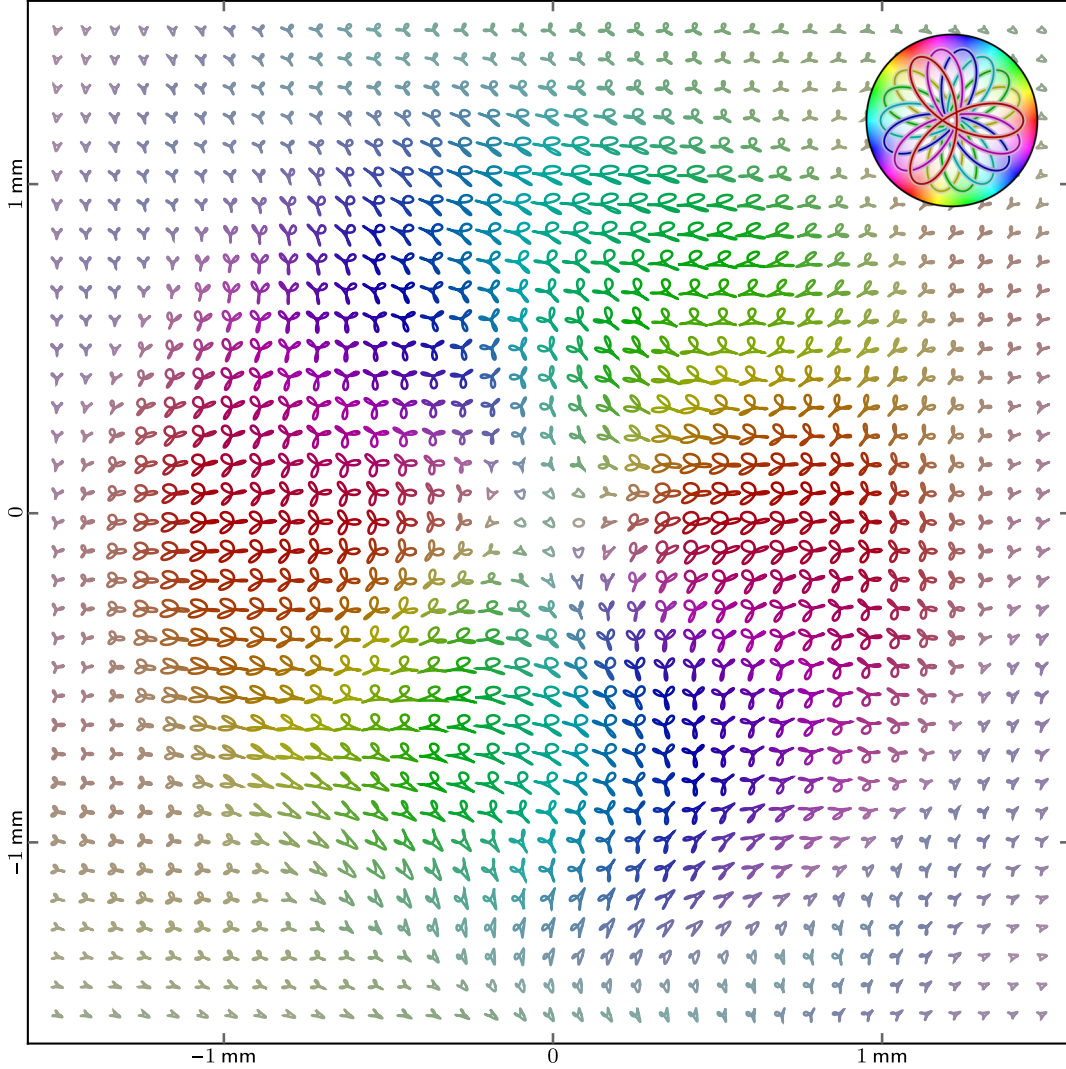


Figure S11 | Reconstruction of Lissajous-figure fields. Reconstruction of the trefoil Lissajous figures from the experimental data at $m = -2$ shown in Fig. 3(d), via the least-squares minimization procedure described in Methods, and assuming unit conversion efficiency χ on NLC2. The figures exhibit some distortion, probably due to interferometric drift over the data collection, which also induces some amount of cross-talk between the reconstructed \mathbf{E}_1 and \mathbf{E}_2 fields (for which evaluating the uncertainty requires further analysis); despite this distortion, the $\gamma = -2/3$ rotation coordination parameter of the trefoil lobes over an azimuthal traversal is clearly visible. The figures are coloured according to their three-fold orientation angle, $\alpha_3 = \frac{1}{3} \arg(T_{3,3}) \pmod{120^\circ}$, with $T_{3,3}$ taken from the Fourier-transformed experimental data, as shown in the inset.